

Divertor studies in nitrogen induced, completely detached H-modes in full tungsten ASDEX Upgrade

F. Reimold, M. Wischmeier, M. Bernert, S. Potzel, A. Kallenbach, H. W. Müller, B. Sieglin, U. Stroth and the ASDEX Upgrade Team

¹ Max-Planck-Institute for Plasma Physics, D-85748 Garching, Germany

E-mail: Felix.Reimold@ipp.mpg.de

Abstract. The first stable, completely detached H-mode plasma in full tungsten ASDEX Upgrade has been achieved. Complete detachment of both targets is induced by nitrogen seeding into the divertor. Two new phases are added to the detachment classification described in [1]: First, the line integrated density increases by about 15 % with partial detachment of the outer divertor. Second, complete detachment of both targets is correlated to the appearance of intense, strongly localized, stable radiation at the X-point. Radiated power fractions, f_{rad} , increase from about 50 % to 85 % with nitrogen seeding. X-point radiation is accompanied by a loss of pedestal top plasma pressure of about 60 %. However, the core pressure at $\rho_{\text{pol}} < 0.7$ changes only by about 10 %. $H_{98} = 0.8 - 1.0$ is observed during detached operation. With nitrogen seeding the ELM frequency increases from the 100 Hz range to a broadband distribution at 1 – 2 kHz with a large reduction in ELM size.

PACS numbers: 52.65.Kj, 52.65.Pp, 52.55.Rk, 52.25.Xz, 52.25.Vy, 52.55.Fa

1. Introduction

In future fusion devices like ITER [2] and DEMO [3] power exhaust is a challenge. At a DEMO relevant, thermal power of $P_{\text{th}} \approx 3 \text{ GW}$ [4] and a midplane power fall off length $\lambda_q \approx 1 \text{ mm}$ [5] parallel power fluxes, q_{\parallel} , of several 10 GWm^{-2} in the SOL of DEMO are to be expected. Accounting for geometry, e.g. flux expansion and tilted targets, a reduction by a factor 100 in the power flux to the targets can be achieved [6]. However, the remaining power flux to the divertor target on the order of several 100 MWm^{-2} is still well above the specified steady-state material limit, which is 10 MWm^{-2} for the ITER [7] and probably lower for the DEMO [8, 9] divertor target.

For target protection in DEMO 70 % of the heating power $P_{\text{H}} = 650 \text{ MW}$ are foreseen to be exhausted via radiation in the confined region, $P_{\text{rad,core}}$, by seeding of high-Z impurities like argon or krypton [10]. If DEMO operates in H-mode the core radiation is limited by the minimum power crossing the separatrix into the SOL, P_{sep} , necessary to stay above the H-L threshold [11]. The remaining power in the SOL needs to be reduced by SOL and divertor radiation from low-Z impurities like nitrogen in order to ensure operation with radiated power fractions, $f_{\text{rad}} = P_{\text{rad}}/P_{\text{H}}$, above 95 % and a detached divertor for target protection. A good characterization and understanding of divertor detachment in H-mode plasmas with significant power fluxes to the divertor is crucial in order to test the theoretical models and identify missing physics.

Operation at high values of f_{rad} including

detached targets in H- and L-mode has been studied in a number of tokamaks [?, 12, 13, 14, 15]. Detached H-mode plasmas have been demonstrated on JT-60U [16, 17], full carbon JET [18], ITER-like wall JET [19], C-Mod [20], DIII-D [21, 22] and full-carbon ASDEX Upgrade, AUG [23, 24]. So far most dedicated detachment studies in full tungsten AUG focused on L-Mode density ramps [1, 25, 26, 6, 27]. In this paper H-mode divertor detachment at $P_{\text{H}} = 6 - 12 \text{ MW}$ is investigated. We focus on the application of impurity seeding to vary the radiated power in the divertor, $P_{\text{rad,div}}$, with nitrogen as a seed impurity. We report on the first stable, completely detached H-modes in full-W AUG. Our experiments showed for the first time that an X-point MARFE-like radiation is intimately coupled to complete detachment with nitrogen seeding in full tungsten AUG. Previous observations of X-point radiation close to detachment in JT-60U [28, 29] and C-Mod [30] did not state a stable steady-state or controllability. We will show that the X-point radiation in the AUG H-mode detachment studies is stable, reproducible, reversible and thus controllable. We will also show that, in contrast to full carbon AUG [31, 32], complete detachment of the outer target is not associated to the occurrence of an H-mode density limit [33] in the full tungsten AUG. Accompanying modeling with SOLPS is discussed in [34].

Section 2 defines the term detachment as used in this paper. Section 3 describes the experimental parameters of the H-mode discharges in this study. A brief summary of the detachment evolution is given in Section 4 and a detailed description of the plasma properties during

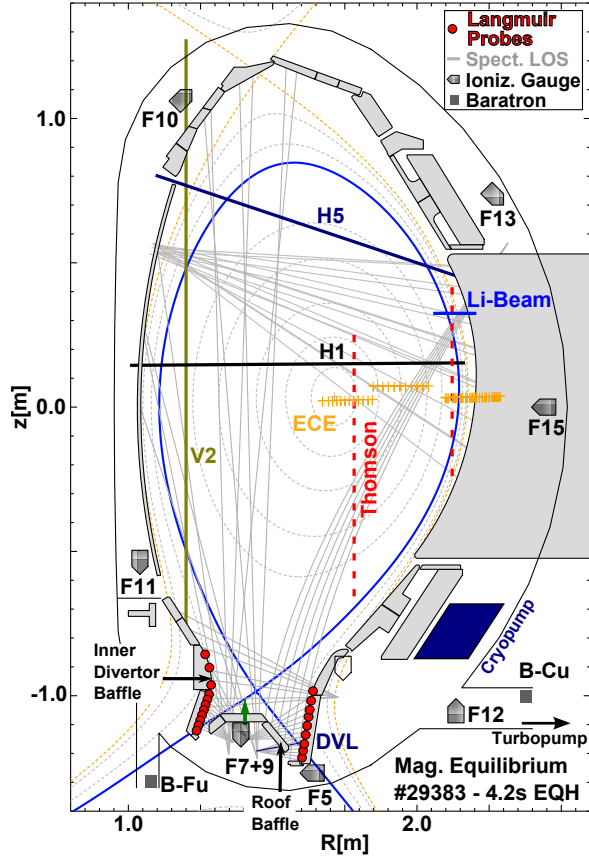


Figure 1 – Diagnostics at AUG: F* are ionization gauges, B* are baratrons, V* and H* are interferometer chords. Target Langmuir probes, spectroscopy lines of sights, electron cyclotron emission measurement locations (ECE), Thomson scattering volumes and the Li-beam geometry are shown as well.

this evolution is given in Section 5. Section 6 shows observations in the pedestal region, on confinement and ELMs during the transition to detachment. Section 7 discusses the experimental observations, gives a possible interpretation and derives conclusions. A summary is given in Section 8.

2. Detachment

The parallel power flux density to the target is given by

$$q_{\parallel} = \underbrace{n_{e,t} c_s \gamma_{sh} k_B T_{e,t}}_{\propto p_{e,t} T_{e,t}^{0.5}} + \underbrace{n_{e,t} c_s E_{pot}}_{\propto p_{e,t} T_{e,t}^{-0.5}} \quad (2.1)$$

where γ_{sh} is the heat sheath transmission factor, $n_{e,t}$ and $T_{e,t}$ are the electron density and temperature in front of the target, c_s is the sound speed and $E_{pot} \approx 15.8$ eV is the potential energy released per ion when recombining to neutral deuterium molecules on the target plate [7].

In present day devices power exhaust requirements are met already in the so-called high-recycling regime due to the reduction of $T_{e,t}$ via (impurity) radiation and ionization energy losses alone. A value of $T_{e,t} \approx 5$ eV suffices for target protection at the experimental densities in devices like AUG. The potential energy flux can be neglected and detachment is not required. Higher P_{SOL} in ITER and DEMO implies higher recycling and hence higher densities at the target and higher fluxes onto the divertor plate [35]. With radiation cooling to $T_{e,t}$ lower than about 2 eV the deposited potential energy is no longer negligible and exceeds the thermal energy transfer of impinging plasma. Without pressure losses along a fieldline, a further reduction in temperature is coupled to an increase in the potential energy flux to the target and a reduction and/or limitation of the particle flux, i.e. detachment, becomes a prerequisite for power handling [7].

Partial detachment is defined as a parallel pressure loss at and close to the strikepoint [36]. In AUG a good indicator for partial detachment of the outer target is a drop of the controller signal T_{div} [37] below

5 eV. The signal T_{div} is derived from shunt current measurements at the target. Complete detachment is defined as strong parallel pressure loss and close to flat target profiles of the ion saturation current, j_{sat} , and electron temperature, $T_{\text{e,t}}$, along a large portion of the target [24]. The peak heat and particle fluxes are reduced by more than one order of magnitude compared to attached conditions with identical upstream parameters. In AUG a significant reduction in j_{sat} is typically observed along the target up to a distance from the strikepoint of $\Delta S = 10 - 15$ cm. The profiles in the far SOL at the outer target ($\Delta S > 15$ cm) show already low particle fluxes and temperatures even in attached conditions and are marginally affected by detachment. For a completely detached outer target the controller signal T_{div} [38] ranges from 0 to -5 eV. Negative values of T_{div} are likely to result from thermo-electric currents with the divertor as the cold end of a flux tube or a suppression of the Pfirsch-Schlüter currents in the SOL with a detached strikepoint [37]. Completely detached H-mode is defined as H-mode operation with both targets completely detached.

3. Experiment

The H-mode discharges in this study are run at $I_{\text{p}} = 800$ kA and $B_{\text{t}} = 2.5$ T, which sets $q_{95} \approx 5.5$. H_{98} ranges from 0.8-1.05. The ion ∇B -drift points into the lower divertor. The plasma current is chosen such that no disruption mitigation is necessary and additional impurities from massive gas injection in subsequent discharges are

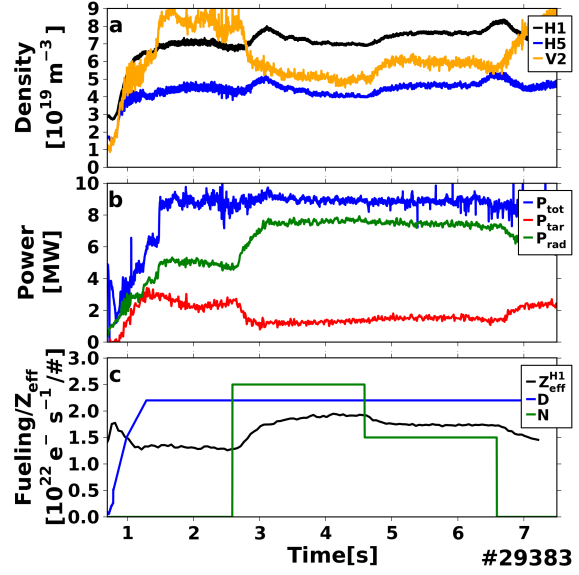


Figure 2 – H-mode detachment experiment #29383: a) Line integrated density (H1: central, H5: edge, V2: Vertical, high-field side SOL (Figure 1)). b) Heating Power (P_{tot}), radiated power (P_{rad}) and power to the target (P_{tar}). c) Fueling/seed rates and the line integrated Z_{eff} along H1.

excluded. The heating power was varied from 6.4 to 11.4 MW with central ECRH of 1.4 MW. The deuterium fueling, Γ_{D} , and nitrogen seeding rates, Γ_{N} , were varied independently in the range of $1 - 3 \times 10^{22} \text{ e}^-/\text{s}$ in order to vary the neutral density in the divertor, $n_{0,\text{div}}$, and the nitrogen concentration of the plasma, c_{N} . Stable impurity concentrations in our discharges are supported by a nitrogen preloaded wall, that minimizes the wall pumping of nitrogen. We achieved preloading with previous nitrogen seeded discharges [?]. Nitrogen dominates \bar{Z}_{eff} during the seeding phase, where \bar{Z}_{eff} is the line integrated Z_{eff} -profile along the central DCN interferometer chord H1, see Figure 1. It increases from 1.3 – 1.4 in the deuterium only reference phase to 1.8 – 2.0 during seeding, see Figure 2. The core nitrogen concentration, c_{N} , varies from a

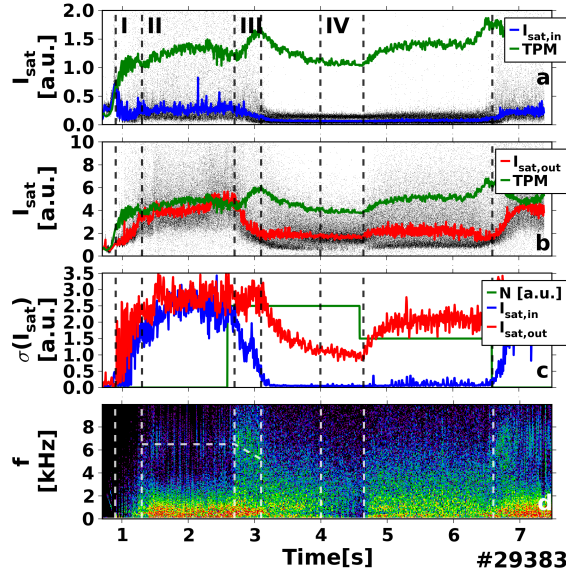


Figure 3 – a)+b) I_{sat} is given in black. Inter-ELM median values $\langle I_{\text{sat}} \rangle_{\text{ELM}}$, are given in blue and red for the inner and outer target respectively. $I_{\text{sat,TPM}}$ is given in green. c) Standard deviation of the I_{sat} signal as a measure of ELM size. d) Power spectrogram of AXUV-diode measurement at the X-point.

pre-seeding level of 0.5 % to 2.0 – 3.0 % during seeding. Other impurities have been measured by CXRS before nitrogen seeding. Their concentration levels are $c_{\text{C}} \approx 0.1$ % and $c_{\text{He}} \approx 0.5$ %. It has to be noted, that the presented experiments did not attempt to minimize the core impurity content. Figure 2 shows time traces of the main control and plasma parameters of the exemplary discharge #29383. The general observations described in this paper are not particular to this discharge, but are common to all discharges in this study.

4. Overview of Detachment Phases

This section summarizes how the detachment evolves. It provides a framework for a more detailed analysis of the individual observations of different plasma quantities

in the following sections. Similar to an L-mode detachment classification in [1] the evolution of H-mode detachment can be divided into four phases. The four phases are indicated in Figure 3:

- (i) Onset of detachment
- (ii) Fluctuating state
- (iii) Partial detachment of outer target
- (iv) Complete detachment

Figure 3.a-b show the evolution of the sum of the ion saturation current density measurements in the lower divertor to the inner and outer target $I_{\text{sat}} = \sum_{LP} j_{\text{sat,LP}}$, where $j_{\text{sat,LP}}$ are individual Langmuir probe measurements, see Figure 1. For comparison a two-point model scaling of I_{sat} is also plotted. The scaling is given by $I_{\text{sat,TPM}} = c_{t_0} \bar{n}_{\text{e,edge}}^2$, where $\bar{n}_{\text{e,edge}}$ is the line integrated edge density measured by the edge interferometer (H-5 in Figure 1) as a proxy for the separatrix density and c_{t_0} is a normalization constant chosen such that $I_{\text{sat}} = I_{\text{sat,TPM}}$ at the reference time, t_0 , with attached targets. For discharge #29383 the reference time is $t_0 = 0.9$ s. Experimental I_{sat} values below the scaling indicate pressure loss along fieldlines, i.e. detachment.

I. Onset of Detachment: During the onset of detachment at 0.9 s I_{sat} to the inner target drops below the TPM-scaling and the inner target detaches inter-ELM, already without impurity seeding. The outer target is attached.

II. Fluctuating state: At 1.3 s the inner target is detached and radiative fluctuations at the X-point with a frequency of 6 – 8 kHz appear during inter-ELM phases, see Figure 3.d. During ELMs the inner tar-

get transiently reattaches and the radiative fluctuations vanish. The outer target stays attached.

III. Partial detachment at outer target: With the beginning of nitrogen seeding at 2.7 s the outer target changes from attached to partially detached during inter-ELM phases. At the same time the radiative fluctuations shift gradually from inter-ELM to ELM time intervals, the fluctuation frequency decreases and merges with a broad band due to ELMs in the spectrogram in Figure 3.d. During this transition the ELM size decreases considerably and ELMs do not reattach the inner target anymore, see Figure 3.a-c. Concomitantly, a strong radiation at the X-point is measured by bolometers ($f_{\text{rad}} \approx 85\%$), see Section 5.5, and a (transient) increase in line integrated density by typically 10 – 20 % is observed, see Section 5.6. An increase in line integrated density with detachment is also observed in [16, 36, 39, 40].

With the onset of nitrogen seeding the particle flux to the inner target in the far SOL above the divertor baffle increases by a factor of about 2 (#29924). At 3.1 s the inner target is completely detached along the vertical target component below the divertor baffle. Unfortunately, the coverage and spatial resolution of Langmuir probe measurements in the far SOL was not sufficient in our experiments to determine if the integrated target flux to the inner target, including the far SOL, is reduced or whether j_{sat} is redistributed from the vertical plate near SOL into the far SOL.

IV. Complete Detachment: Starting at 4.0 s the inner target far SOL j_{sat} rolls over. Simultaneously, the bolometer, outer tar-

get Langmuir probes, divertor shunt current and H_α measurements change from broadband, high frequency ELMs to a fluctuating structure with only sporadic clear inter-ELM-like intervals, see Section 6.1. The X-point radiation moves further into the confined plasma and strong Balmer- and NIII-line radiation at the X-point emerges, see Section 5.5. Both spectral lines are indicators of increased ionization inside the confined region. Both targets are completely detached at 4.5 s and particle and power fluxes at both targets are reduced to low levels, see Section 5.1. Midplane profiles of n_e , T_e and T_i show a loss of pressure (60 %) at the pedestal top ($\rho_{\text{pol}} = 0.95$) during complete detachment compared to the non-seeded phase. However, the core pressure inside $\rho_{\text{pol}} < 0.7$ and hence core confinement is only slightly affected. The confinement according to the H_{98} scaling ranges from 0.8-1.0 with complete detachment and 0.85-1.05 in the non-seeded reference phase, see Section 6.

5. Detailed Analysis of Divertor Plasma

In this section the observations during the evolution of detachment with nitrogen seeding are presented in more detail. Each diagnostic group will be discussed along the sequence of the evolution just described.

5.1. Target Profiles

Figure 4 compares representative Langmuir probe and infrared camera target profiles for attached and completely detached conditions in #29383. The profiles of j_{sat} are derived with the assumption of $T_e = T_i$ and

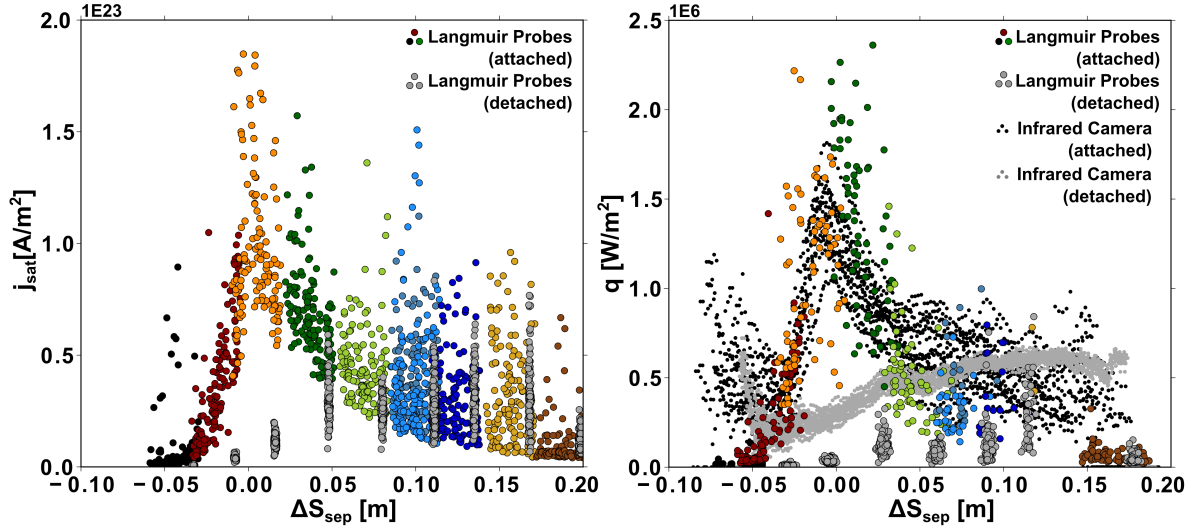


Figure 4 – Inter ELM, outer target profiles of j_{sat} (a) and q_{\parallel} (b) for #29383. Different colors are individual Langmuir probes. The plotted time intervals are 20 – 2.3 s (reference) and 4.0 – 4.5 s (seeded).

Qty	Reduction Factor	
	Inter-ELM	With ELMs
$I_{\text{sat,in/out}}$	5 / 2.5	≤ 100 / 2.5
Average		
$P_{\text{tar,in/out}}$	5 / 2	

Table 1 – Reduction factors of peak fluxes to the targets from attached to completely detached targets are summarized for #29383.

a pure deuterium plasma for the evaluation of the probe data. A sheath heat transmission coefficient $\gamma_{\text{sh}} = 8$ is used for the evaluation of q_t from Langmuir probes. Due to low target plate surface temperature the heat flux can be reliably diagnosed with infrared measurements only around the strike point ($0 \text{ cm} < \Delta S < 5 \text{ cm}$) in our discharges.

In all experiments of this study the inter ELM peak j_{sat} at the outer target has been reduced by approximately one order of magnitude to values below $5 \times 10^{22} \text{ e}^- \text{m}^{-2} \text{s}^{-1}$. At the inner target the peak j_{sat} was reduced to below

$5 \times 10^{21} \text{ e}^- \text{m}^{-2} \text{s}^{-1}$. The inter ELM peak heat flux to the outer target has been reduced by more than a factor of 3 to below 0.5 MWm^{-2} . Table 1 summarizes the reduction of the peak fluxes to both targets from attached to completely detached divertor targets.

The inter-ELM electron temperature measured by Langmuir probes at the target was decreased from $T_e \approx 10 - 30 \text{ eV}$ in attached conditions to $T_e \approx 1 - 2 \text{ eV}$ in detached regions during complete detachment. Probe temperatures below 2 eV are likely to be overestimated [41]. Significant nitrogen content in the divertor plasma can lead to an underestimation of n_e by the Langmuir probes [42].

5.2. Recycling & Line Emission

Taking into account atomic data [43] spectroscopy provides information about the temperature distribution and the spatial distribution of ionization and recombina-

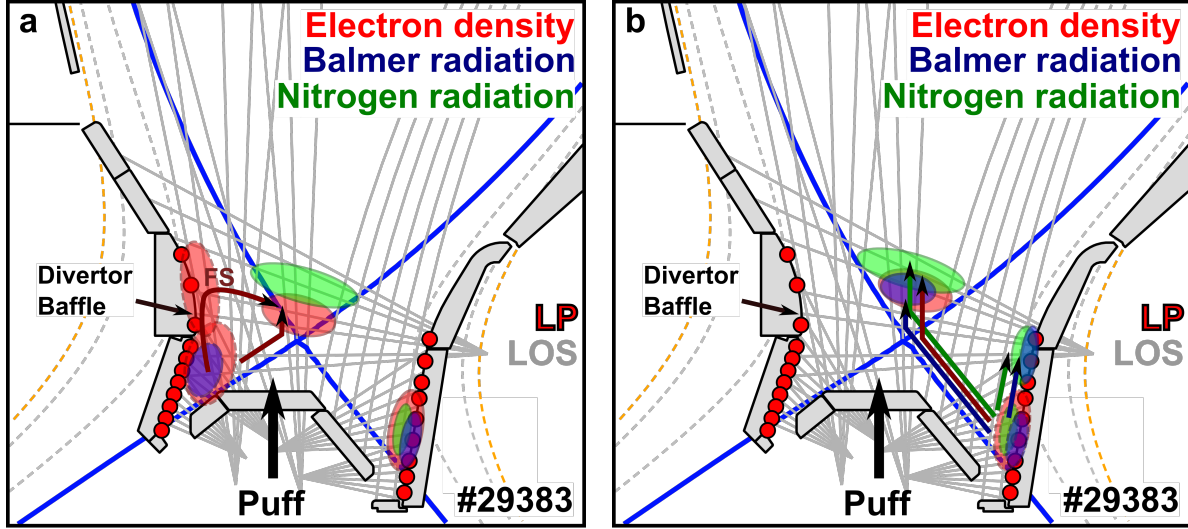


Figure 5 – Divertor evolution during detachment measured by spectroscopy. Active Langmuir probes are shown in red. The divertor spectroscopy lines of sight are shown in grey. a) Transition from attached to fluctuating state (label FS) to partially detached outer target is shown. b) Transition from partially detached outer target to completely detached targets is shown.

tion in the divertor volume. Spectroscopic measurements in our experiments comprise a doublet NIII line at $\lambda = 410.12$ nm as well as the Balmer lines D_δ at $\lambda = 410.05$ nm and D_ϵ at $\lambda = 396.90$ nm. The fractional abundance of the coronal ionization equilibrium of nitrogen peaks at 5 – 10 eV for NIII [43]. Hence, the NIII line emission is an indicator for the ionization region of neutral deuterium. Stark broadening analysis of D_ϵ and D_δ provides the electron density, $n_{e,\text{Stark}}$ in the volume [44].

The changes of the spatial distribution with proceeding detachment of n_e , Balmer, $I_{D_{\delta,\epsilon}}$, and NIII, I_{NIII} , line intensity in the divertor volume is shown schematically in Figure 5. From attached targets to the fluctuating phase with a detached inner target, the region of highest n_e moves along the inner target to the divertor baffle, see label 'FS' in Figure 5. The particle flux to the vertical inner target below the divertor

baffle is reduced to very low inter ELM values ($j_{\text{sat}} \leq 5 \times 10^{21} \text{ e}^- \text{m}^{-2} \text{s}^{-1}$). The high density region in the inner divertor is also seen to move away from the inner target along the separatrix towards the X-point. The Balmer radiation in the inner divertor is still concentrated along the target plate. The outer divertor stays attached with an Eich profile [5] peaked at the strikepoint and the target plate, both in n_e and line radiation.

With nitrogen seeding the outer divertor detaches partially. The inner divertor volume below the X-point height does not show significant line emission ($I < 5 \times 10^{18} \text{ Ph sr}^{-1} \text{m}^{-2} \text{s}^{-1}$) from this point on. Stark broadening measurements limit $n_{e,\text{Stark}}$ to below $5 \times 10^{19} \text{ m}^{-3}$ indicating the absence of significant ion particle fluxes and ionization in this region. The vertical line of sight adjacent to the inner target plate show a reduction in I_{D_δ} by a factor of

10, while the density at the divertor baffle drops from $n_{e,\text{Stark}} = 5 - 6 \times 10^{20} \text{ m}^{-3}$ to $2 - 3 \times 10^{20} \text{ m}^{-3}$. The Langmuir probes at the inner target above the baffle measure an increase in j_{sat} of up to a factor of 4 in the far SOL, while j_{sat} to the vertical target decreases further. A similar increase in j_{sat} in the outer far SOL is seen in similar discharges with wider Langmuir probe coverage (#30308). The increase in local recycling at the inner far SOL plate seems to be in contradiction to neutral flux measurements of ionization gauges behind the heat shield (F11) and far SOL electron density measured by a vertical CO₂-interferometer chord (V2) on the high-field side, HFS, which are decreasing with the onset of nitrogen seeding, see Figure 1 and Section 5.6.

At the outer target the strikepoint $n_{e,\text{Stark}}$ reduces by a factor two and I_{D_δ} increases along the whole outer target by a factor of 4-6 with a profile that is peaked around the strikepoint. After an initial increase in the NIII line emission along the whole outer target by a factor of 3 the peak emission moves from the strikepoint along the target into the far SOL. Simultaneously, a second emission region moves to the X-point and NIII emission emerges above the X-point inside the confined plasma.

With the transition from partial detachment to complete detachment at the outer target the peak Balmer and NIII-emission move further up the outer target plate and the profiles flatten out. Concomitantly, the NIII emission region above the X-point moves further upward and below strong Balmer radiation emerges inside the separatrix. The region with high n_e coincides in this phase with the Balmer emission

zone. The electron density profile along the outer target is flat when determined by spectroscopy with $n_{e,\text{Stark}} \approx 3 \times 10^{20} \text{ m}^{-3}$ and almost flat in Langmuir probe measurements with $n_{e,\text{LP}} = 2 - 4 \times 10^{19} \text{ m}^{-3}$. The Langmuir probe measurements take into account the variation of the collecting area of flush mounted probes [45, 46]. The difference in the electron density measurements from Langmuir probes and Stark broadening indicates that the maximum density in the inner divertor has moved away from the target surface into the divertor volume. Langmuir probes show a roll over of j_{sat} in the far SOL and $n_{e,\text{Stark}}$ at the inner divertor baffle reduces again by a factor of 2.

The presence of significant D_δ Balmer radiation inside the confined plasma indicates low temperatures below 5 eV comparable to observations with Thomson scattering measurements in Ref. [36]. Balmer line ratio measurements of $\frac{D_\epsilon}{D_\delta}$ for lines of sight that pass through the X-point region have been analyzed with ADAS photon emission coefficients [43] and indicate temperatures below 1 eV and a recombining plasma.

Limiter spectroscopy at AUG observes the low-field side, LFS, limiter from the top part of the HFS limiter, see Figure 1. The limiter spectroscopy includes D_ε, NII, NIII and WI lines. The intensity of these lines changes with the application of nitrogen seeding. The nitrogen line intensities at the limiter increase with nitrogen seeding by about a factor of 4. Tungsten and Balmer line intensities decrease with nitrogen seeding, indicating less tungsten influx from the limiters despite increased nitrogen recycling. The limiter I_{D_ϵ} evolution scales with the neutral flux measurement behind

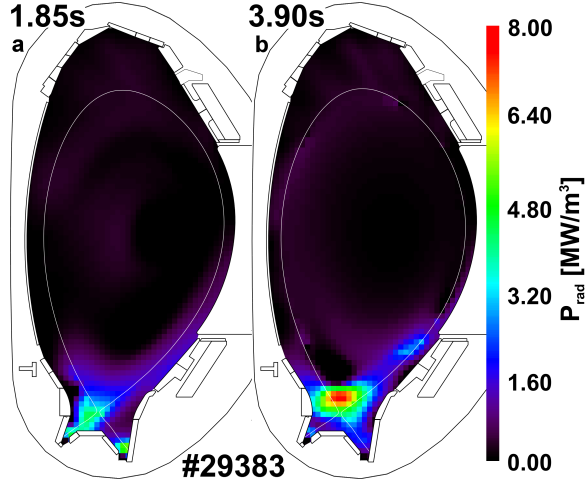


Figure 6 – Tomography of bolometer measurements without (1.85 s) and with (3.9 s) nitrogen seeding. The radiation characteristic changes from detached inner divertor to stable, MARFE-like X-point radiation.

the HFS (F11) and the far SOL density measurement (V2), see Section 5.6. It has to be noted that the limiter lines of sight do not end in tile gaps as viewing dumps and reflections at the metallic limiter surfaces could be significant.

5.3. Radiation

Radiation in the divertor volume disperses the power to the target and reduces the plasma temperatures to values necessary for detachment. Bolometer measurements indicate the location of radiating regions. In AUG the total radiated power, P_{rad} , is measured by foil bolometers. The analysis is hampered by the fact that high frequency ELMs cannot be resolved by the foil bolometers. Furthermore, possible reflections at plasma facing components, PFCs, and inside the bolometer cameras are not taken into account in the analysis [47]. At AUG a fast evaluation of P_{rad} based on bolometric measurements and geometric assumptions is used to determine

$f_{\text{rad}} = \frac{P_{\text{rad}}}{P_H}$. A comparison of the fast evaluation and tomographic inversions is used to recalibrate the fast P_{rad} in this work. With recalibration P_{rad} fulfills the quasi-steady-state power balance (5.1) during N-seeding to an accuracy of about 10% in all our discharges with the same calibration factor.

$$P_H \approx P_{\text{tar}} + P_{\text{rad}} \quad (5.1)$$

where P_{tar} is the power to the divertor target measured by infrared camera.

In the detachment studies f_{rad} increases from 0.5-0.6 in unseeded reference phases to 0.8-0.9 during nitrogen seeding. A tomographic reconstruction of P_{rad} of #29383 without and with N-seeding is shown in Figure 6.

The evolution of the total radiation in the bolometer measurements is similar to that of the NIII-line emission observed with divertor spectroscopy: In the non-seeded phase the bulk of the radiation stems from the inner divertor, see Figure 6.a. With the onset of nitrogen seeding the dominant radiation first shifts to the volume of the partially detached outer divertor and then to the X-point as the divertor detaches completely, see Figure 6.b. The radiation moves into the confined plasma above the X-point at the same time NIII and Balmer line radiation is spectroscopically observed inside the confined region. This X-point radiation is correlated to the maximum pressure loss along the separatrix from upstream to the target, an upstream pressure loss at the pedestal top, see Section 6, and completely detached targets with ELMs replaced by broadband fluctuations, see Section 6.1.

Similar observations of strong radiation losses at the X-point during detachment have already been made in a number of experiments [48, 49, 50, 51, 19]. However, the experimental observations did locate the X-point radiation either outside of the separatrix or did not comment on the stability. In the detachment studies presented here the X-point MARFE-like radiation proved to be reproducible and stable.

Experiments indicate that the X-point radiation is not steady-state in our feed-forward seeding approach as there is an ongoing upward movement. However, the slow evolution of the radiation on timescales of 1 s and the experimental observation that the X-point radiation reacts on a time scale of several 100 ms to a reduction of the seeding rate should allow for a feedback control of the X-point radiation position using the nitrogen seeding rate as the actuator and bolometer lines of sight as a controller.

5.4. Radiative Fluctuations

Fast AXUV diode bolometers at AUG measure with 200 kHz time resolution [52] and provide insight into fast radiative processes. The diodes are not absolutely calibrated and can not be used for absolute radiated power analysis. The AXUV diodes show radiative fluctuations in AXUV chords close to the HFS X-point, see Figure 4.d. During the fluctuating state the observations are consistent with [27].

The fluctuations are first observed in inter-ELM periods when the inner divertor is detached along the vertical target. ELMs transiently reattach the inner target and

the radiative fluctuations disappear during the ELM. With increasing detachment during nitrogen seeding the outer divertor detaches first inter-ELM and then completely. Accordingly, the radiative fluctuations switch from inter-ELM to ELM time intervals and vanish with detachment of the outer target. Hence, the appearance of the radiative fluctuations seems to correlate with a simultaneously detached inner target and attached outer target. The frequency of the radiative fluctuations decreases with nitrogen seeding as shown in Figure 4.c. In Ref. [27] a connection of the radiative X-point fluctuations with a high field side high density, HFSHD, in the inner divertor is observed. In our experiments the radiative X-point fluctuations are clearly distinguishable in the AXUV diode signals from the broadband ELMs until the HFSHD is completely eliminated by nitrogen seeding, see Figure 8 and Section 5.6.

5.5. Tungsten Erosion

In AUG tungsten is produced by plasma-wall interaction at the main chamber wall and in the divertor. Tungsten erosion and PFC degradation is a concern for ITER. Tungsten is not fully ionized in the core plasma and will effectively reduce the energy confinement by line radiation. The maximum allowed tungsten concentration is therefore limited in future fusion devices. In AUG too high tungsten core contamination will additionally lead to the occurrence of tungsten accumulation and a radiative collapse of the plasma with a subsequent disruption. In the presented discharge scheme the core tungsten concen-

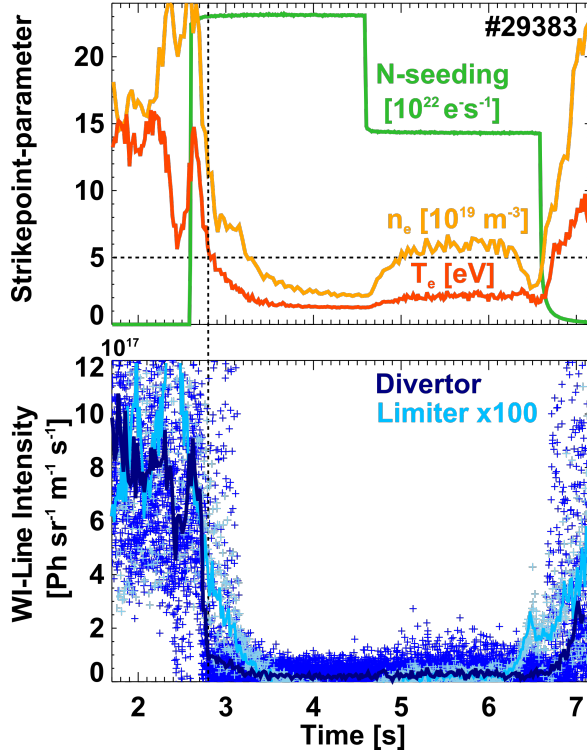


Figure 7 – Fast cooling of the divertor by a fast ramp-up of the nitrogen seeding leads to an almost complete suppression of gross W-erosion at the divertor target and the low-field side limiter. The critical temperature at the observed region is $T_e = 5$ eV.

tration is moderate ($c_W < 5 \times 10^{-5}$) if fast cooling of the divertor by a prompt increase of the nitrogen seeding rate to levels in the range of $1 \times 10^{22} \text{ e}^- \text{s}^{-1}$ is applied. Fast cooling avoids enhanced tungsten influx from sputtering by nitrogen at the divertor plate. Spectroscopic measurements in the divertor, DVL in Figure 1, and at the LFS limiter use the WI line at $\lambda = 400.9$ nm as a measure of the tungsten influx (S/XB). Inter-ELM tungsten influx in the outer divertor close to the strikepoint is suppressed as soon as the Langmuir probe at this position measures $T_e \leq 5$ eV, see Figure 7. The reduction in ELM-size with nitrogen seeding is also very beneficial as enhanced tungsten influx during ELMs is no longer observed with completely detached divertor

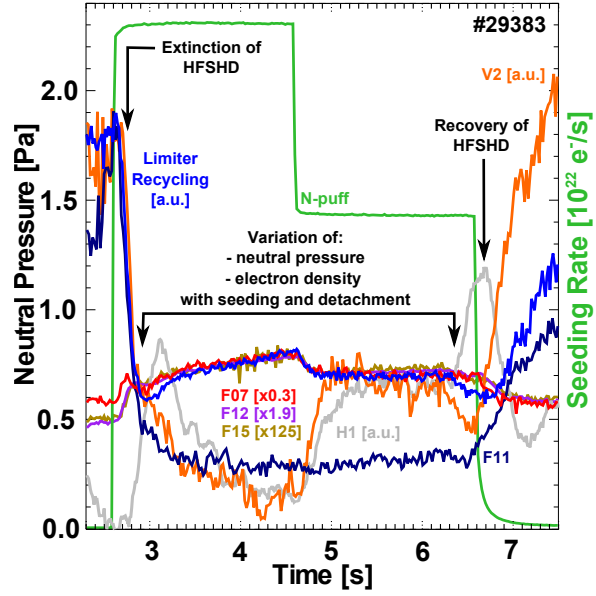


Figure 8 – Timetraces of neutral pressure measurements, spectroscopic measurements of limiter recycling, nitrogen seeding rates as well as of the line integrated high-field side density (V2) and central density (H1) are shown.

in our experiments. Limiter spectroscopy at the LFS limiter also observes a reduction of tungsten influx from the main chamber walls with nitrogen seeding - both inter-ELM and due to ELMs.

The fast cooling of the divertor leads to a fast transition to detachment. This is not desirable for diagnosing the divertor plasma and the detachment transition. Attempts at discharges without fast cooling, but with a slow ramp up of nitrogen seeding tended to disrupt due to a radiative collapse induced by a tungsten accumulation.

5.6. Fueling, Neutral pressure evolution and High field side high density

The neutral pressure distribution in AUG is monitored by a number of poloidally distributed ionization gauges [53] as shown in Figure 1. With nitrogen seeding the fact that the gauge sensitivity for N_2 is

approximately three times higher than that for D₂ [54] makes a quantitative analysis difficult.

Timetraces of the neutral pressure at selected poloidal locations are shown in Figure 8. The neutral pressure changes increases by roughly 60 % from attached outer target at 2.5 s to a completely detached divertor at 4.5 s. Most gauges, including the ones in the main chamber (F15), follow the trend of the pump chamber gauge (F12) and increase with nitrogen seeding and detachment, see Figure 8. Despite the transition to complete detachment no loss of neutral compression is observed, i.e. the ratio of F12 to F15 does not change. In future studies the effect of complete detachment on the pumping of helium ash in a future reactor will have to be assessed in detail. Gauges behind the HFS limiter at the central column (F11) behave different: Before nitrogen seeding with the transition from onset of detachment to fluctuating state a HFSD region is formed in the far SOL of the inner divertor at and above the divertor baffle. Along with spectroscopy [55] and the vertical CO₂-interferometer chord V2 [56], the HFS limiter gauges observe the HFSD by an increase in neutral flux, see Figure 8 before 2.6 s. With the onset of nitrogen seeding and partial detachment of the outer target our experiments show a drop of this HFSD by a factor of 2-4 accompanied by a neutral pressure drop by a factor 3-4 at the HFS limiter gauge (F11), see Figure 8 from 2.6 – 3.0 s, and by about 25 – 50 % below the inner divertor (B-Fu in Figure 1). Comparison of the ionization gauges with baratrons shows that there is agreement of the inner divertor baratron with the HFS

limiter gauges throughout the fluctuating phase. The correlation of the baratron and the HFS limiter gauges is surprising, because neutral baffling behind the inner divertor structure is tight, see Figure 1, and the gauges below the roof baffle in the PFR do not show a similar increase in neutral pressure, see Section 7. This indicates a possible role of a neutral conductance of the inter-tile gaps for a correct description of the neutral distribution in the inner divertor.

The decrease in the HFSD is correlated in time to the increase of line integrated electron density by 10 – 20 % as well as a drop in main chamber recycling. The timescales of these changes are also comparable, see Figure 8.a and Section 4. The concomitance suggests not only a change in the recycling pattern close to the plate, but also a correlated impact on core plasma fueling. Similar observations of increasing density with detaching targets are made in Ar- and Kr-seeded H-modes and in L-mode detachment studies in AUG [40, 1] as well as in JET H-mode density limit studies [19]. The subsequent drop of the line integrated electron density seems to be related to the appearance of low temperatures, i.e. Balmer radiation, at the X-point as also seen in Ref. [48]. The reason for this reduction in fueling efficiency is yet unclear and could either be attributed to a change of the ionization inside the separatrix due to the high density region at the X-point or due to increased radial transport that could be triggered by plasma drifts and strong local gradients at the X-point. In contrast to Ref. [48] a pronounced decrease of divertor retention of nitrogen does not seem occur in our experiments.

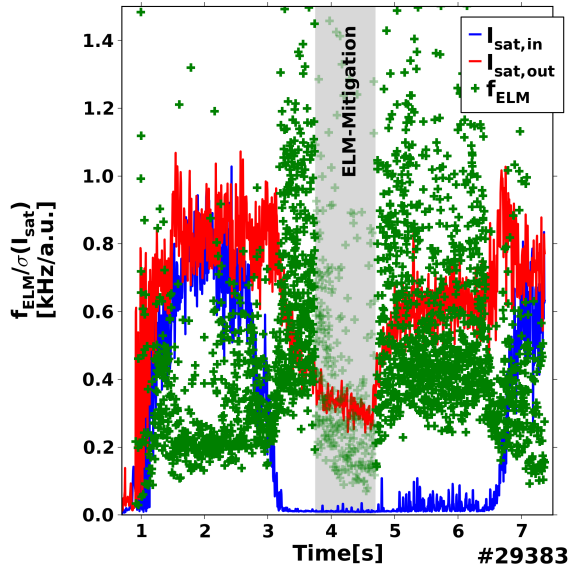


Figure 9 – Standard deviation of I_{sat} from inner (blue) and outer (red) divertor is plotted as measure for the ELM size in the divertor. The ELM frequency (green) increases dramatically with nitrogen seeding. The shaded region of the ELM frequency is an interval without clear ELM signatures but broadband, high frequency fluctuations.

6. ELMs, Upstream Profiles & Confinement

6.1. ELMs

In our experiments ELMs are of type-I and type-III in the initial reference, unseeded phase. Figure 9 shows the ELM frequency and the fluctuation level of I_{sat} at both divertor targets as measure of the ELM size. Consistent with [24, 32] type-I ELMs are gradually replaced by type-III ELMs with the onset of nitrogen seeding. The frequency of the type-III ELMs increases from an initial $f_{\text{ELM}} \approx 200$ Hz. With detachment of the outer target f_{ELM} rises further into the kHz-range and the ELM size decreases significantly. At the same time the rather well defined ELM frequency changes into a broadband

frequency distribution. In discharges with low X-point position the ELMs transform into high-frequency, broadband fluctuations without fixed frequency and without clear ELM signatures (3.5 – 4.75 s). These incoherent fluctuations can be observed in the fast diode bolometers, the target shunt current and the divertor D_α diode measurements. The transition from ELMs to broadband fluctuations is correlated to a pressure loss in the pedestal and the appearance of Balmer radiation during the X-point radiation phase, see Section 6.2 and Section 5.5.

6.2. Upstream profiles & confinement

Detachment and radiation inside the confined plasma is usually accompanied by a loss of confinement. The reduced confinement is one concern for operation of a future fusion device with completely detached divertor. In some of our discharges significant initial confinement improvement of 10 – 20 % in $H_{\text{IPB98(y,2)}}$ [57] with nitrogen seeding can be observed before the transition to a detached outer target (e.g. #29925). Detachment of the outer target is associated with a reduction of H_{98} by about 10 – 20 %. The confinement improvement by nitrogen seeding is probably masked in most discharges by a confinement loss due to detachment and/or the change of ELMs. We analyze the midplane profiles of n_e and $T_{e,i}$ of discharge #29384 in order to examine the confinement loss observed in H_{98} . #29384 differs from #29383 only in 33 % higher deuterium fueling. Figure 10 shows the profiles for attached to completely detached conditions. The midplane profiles change with nitrogen seeding and evol-

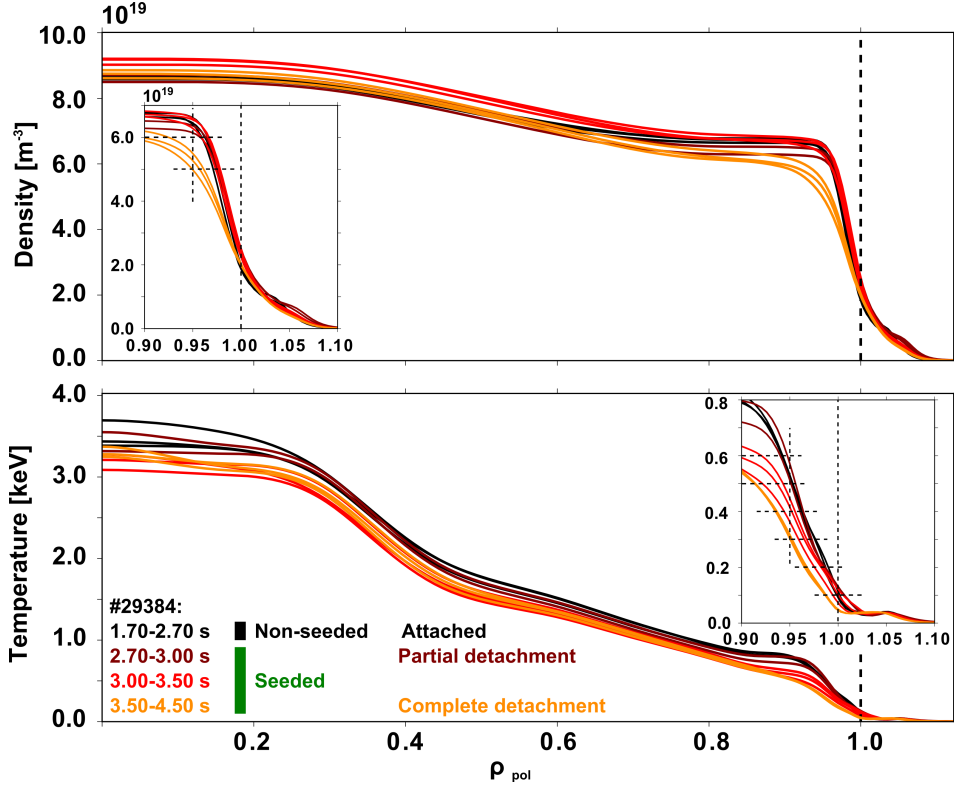


Figure 10 – Midplane profiles of electron density and temperature from non-seeded reference phase (black - 1.7 – 2.7 s) to completely detached phase (orange - 3.5 – 4.5 s) of discharge #29384. Profiles are ELM-synchronized and only inter-ELM measurements are shown, except for the completely detached phase. The ion temperature behaves similar to the electron temperature and is not shown for clarity.

ing detachment. First, with the transition to a detached outer target (2.7 – 3.5 s) the pedestal ($\rho_{\text{pol}} = 0.95$) temperature, $T_{\text{e,ped}}$, reduces by about 40 % while the pedestal density, $n_{\text{e,ped}}$, does not change after a transient increase. Hence, the pressure reduction during this phase is about 40 %. Once the outer divertor is completely detached and Balmer radiation appears inside the confined region at the X-point (3.5–4.5 s) $n_{\text{e,ped}}$ is reduced by about 25 % and $T_{\text{e,ped}}$ is reduced by another 15 %. Hence, the pedestal top pressure is largely reduced compared to the unseeded values by about 60 %. A similar magnitude of reduction has been observed for X-point radiation in Ref. [48]. The pedestal top values stabilize at $n_{\text{e,ped}} \approx 5 \times 10^{19} \text{ m}^{-3}$,

$T_{\text{e,ped}} \approx T_{\text{i,ped}} \approx 300 \text{ eV}$ for #29384. The ion temperature (not shown) and the electron temperature are well coupled during this evolution.

Despite the reduction in pedestal top pressure and a loss in H_{98} it is important to note that the core profiles inside $\rho_{\text{pol}} < 0.7$ change only by about 10 % even during complete detachment. The profile data suggests increased gradients in the region from $0.8 < \rho_{\text{pol}} < 0.95$ that recover most of the pedestal top pressure loss towards the core.

The loss in pedestal top pressure is accompanied by a loss of separatrix pressure. The separatrix pressure drop cannot be accurately quantified with the accuracy of the magnetic field reconstruction and the avail-

able experimental profiles of n_e , T_e and T_i . However, the pressure loss at the divertor target is significantly larger during detachment ($> \times 10$) than that of the upstream pressure just described ($< 60\%$).

7. Discussion

The experiments in H-mode did show that the classification of detachment that was found in L-Mode [1] applies to H-Mode with the addition of an intense X-point MARFE-like radiation in the confined plasma during outer target detachment. In H-mode complete detachment has not been achieved with deuterium fueling only [47] and additional seeding of the low-Z impurity nitrogen is required.

Section 5.6 shows that the increase in line integrated density at the onset of partial detachment is accompanied by a decrease in the HFSHD and local recycling at the inner divertor baffle indicated by lower neutral pressures at the HFS heatshield. Similar observation have been made in L-mode detachment studies [1]. A correlation of the neutral pressure measured by the HFS heatshield ionization gauges (F11) and the baratron below the inner divertor (B-Fu) with the HFSHD implies a significant neutral conductance from the recycling region in front of the inner target to the volume behind the inner target. As the baffling from the HFS limiter to the volume behind the inner target is tight and no increase in neutral pressure below the roof baffle is observed it is most likely that the local recycling at the inner divertor baffle is connected to the baratron via the slits in between tiles at the inner target. This can have

implications on the recycling of neutrals along the whole inner target and might redistribute recycling flux into the far SOL. This also emphasizes the importance of a sophisticated neutral conductance model in future modeling of these plasmas.

The power entering the inner divertor is a measure of the recycling that can be sustained and hence of the level of density (HFSHD) that can be maintained. Increased radiation losses in the SOL and divertor volume due to nitrogen seeding drop the available power for ionization and are probably responsible for the reduction of the HFSHD. Neutrals from the inner divertor should now be able to penetrate through the cold, less dense inner divertor volume to the outer divertor and to the X-point. Local fueling of the central plasma across the X-point should be increased and could lead to the increase in line integrated density and fueling efficiency. A pending question is why the density increase is only transient in most of our discharges. Additional neutrals in the outer divertor should also facilitate the partial detachment of the outer target that occurs at this point.

Recently, a change in blob transport in the SOL with detachment of the outer divertor has been proposed [58]. Our observations of increasing j_{sat} measurements in the far SOL with nitrogen seeding could be explained by an increased transport of particles into these far SOL fluxtubes. In the inner divertor the far SOL j_{sat} might also increase, because the shielding of the target by the HFSHD and possible volume recombination cease with outer target detachment. This would reconcile the increase in j_{sat} with the decrease in the neutral flux measurements at the HFS

heatshield (F11).

Significant Balmer radiation ($I_{D_\delta} \approx 1 \times 10^{19} \text{ Ph sr}^{-1} \text{ m}^{-2} \text{ s}^{-1}$) inside the confined plasma at the X-point during complete detachment indicates $T_e \leq 5 - 10 \text{ eV}$ and a further increase of neutral deuterium density inside the X-point. This increase could be due to an enhancement in neutral penetration across the X-point due to the local radiation cooling by the X-point radiation and/or volumetric recycling at the X-point, i.e. local ionization and recombination inside the X-point radiation region. Upstream measurements of $T_{e,\text{sep}} \approx 50 - 100 \text{ eV}$ imply strong parallel temperature gradients in the confined plasma close to the separatrix induced by the power losses due to X-point radiation. Observed strong density and temperature gradients at the X-point might lead to increased transport taking into account recent considerations for snowflake divertors [59].

The presented experimental evidence shows that a stable operation with complete detachment induced by nitrogen seeding in AUG H-modes is possible. A back transition to L-mode due to an H-mode density limit was not observed in our experiments with completely detached outer target. A new regime in H-mode with intense, very localized radiation at the X-point similar to [16, 60, 29] is found in full-W AUG during detachment.

Overall, this plasma regime is very attractive for a future fusion reactor as it features almost unaffected core plasma profiles for $\rho_{\text{pol}} < 0.7$ with reduced pedestal parameters ($n_e, T_{e,i}$), increased gradients in the region $0.7 < \rho_{\text{pol}} < 0.95$ that recover the

pedestal pressure loss. In addition, the intense and stable X-point radiation reduces the power flux into the divertor and the ELM size is reduced to a level where no clear ELM signatures at the targets can be observed. The reduced separatrix pressure and ELM size facilitate detachment of the divertor by relaxing the upstream conditions and avoiding transient reattachment. The unhampered core profiles pose the question if for DEMO the H_{98} reduction alone should be interpreted as a performance loss. A reduced pressure at the pedestal top might be acceptable or even preferential if the core plasma parameters are unchanged and provide the same active volume that features plasma parameters necessary for fusion reactions. Further analysis, including the impact of the impurity concentration on dilution and plasma performance, similar to Ref. [61] will be necessary for a sound extrapolation to a future reactor plasma scenario.

8. Summary

A set of experiments with nitrogen seeding has shown that in AUG complete detachment of both divertor targets can be achieved in a stable and controlled H-mode with acceptable core impurity levels, a very beneficial regime of intense X-point radiation and reduced pressure at the pedestal top whilst almost unchanged core plasma pressure ($\rho_{\text{pol}} < 0.7$). ELMs change with nitrogen seeding from type-I to high frequency, broadband type-III ELMs with reduced size. ELM mitigation has been observed during complete detachment.

High radiation losses at and above the X-point are beneficial for power dispersal

across the whole first wall - including the main chamber wall. Analysis of the X-point radiation with visible spectroscopy revealed low temperatures and high (neutral) densities above the X-point inside the confined plasma that require the existence of large poloidal gradients on closed field lines during detachment. The reduced pressure at the separatrix and the increased gradients in the edge plasma ($0.7 < \rho_{\text{pol}} < 0.95$) facilitate divertor detachment while maintaining the core plasma performance. This regime might be a very interesting candidate for a future fusion device, where high radiative fractions inside the confined plasma will be necessary to handle the power exhaust in the SOL and divertor. Accompanying SOLPS modeling of these discharges is able to recover most of the observed phenomena [34].

Acknowledgements

Special thanks to B. Lipschultz for fruitful discussions and support. This work has been carried out within the framework of the EUROfusion Consortium and has received funding from the European Union's Horizon 2020 research and innovation programme under grant agreement number 633053. The views and opinions expressed herein do not necessarily reflect those of the European Commission.

References

- [1] S. Potzel, et al. *Nucl. Fusion*, 54(1):013001, January 2014.
- [2] M. Shimada, et al. *Nuclear Fusion*, 47(6):S1–S17, June 2007.
- [3] P. Batistoni. Technical Report CCE-FU 49/6., March 2010.
- [4] V. Mukhovatov, et al. *Nuclear Fusion*, 47(6):S404–S413, June 2007.
- [5] T. Eich, et al. *Phys. Rev. Lett.*, 107(21):215001, November 2011.
- [6] C. S. Pitcher and P. C. Stangeby. *Plasma Phys. Control. Fusion*, 39(6):779, June 1997.
- [7] A. Loarte, et al. *Nuclear Fusion*, 47(6):S203–S263, June 2007.
- [8] A. R. Raffray, et al. *Fusion Engineering and Design*, 85(1):93–108, January 2010.
- [9] Y. Ueda. *Plasma and Fusion Research*, 5:S1009–S1009, 2010.
- [10] A. Kallenbach, et al. *Plasma Physics and Controlled Fusion*, 55(12):124041, December 2013.
- [11] F. Ryter, et al. *Nucl. Fusion*, 53(11):113003, November 2013.
- [12] H.-S. Bosch, et al. *Plasma Phys. Control. Fusion*, 39(11):1771, November 1997.
- [13] A. W. Leonard, et al. *Physics of Plasmas*, 5(5):1736, 1998.
- [14] J. A. Goetz, et al. *Physics of Plasmas*, 3(5):1908, 1996.
- [15] J. Rapp, et al. *Nuclear Fusion*, 52(12):122002, December 2012.
- [16] N. Asakura, et al. *Nucl. Fusion*, 36(6):795, June 1996.
- [17] N. Asakura, et al. *Journal of Nuclear Materials*, 241–243:559–563, February 1997.
- [18] A. Loarte, et al. *Nucl. Fusion*, 38(3):331, March 1998.
- [19] A. Huber, et al. *Journal of Nuclear Materials*, 438, Supplement:S139–S147, July 2013.
- [20] B. Lipschultz, et al. *Fusion science and technology*, 51(3):369–389, 2007.
- [21] T. W. Petrie, et al. *Journal of nuclear materials*, 363:416–420, 2007.
- [22] M. E. Fenstermacher, et al. *Journal of Nuclear Materials*, 241–243:666–671, February 1997.
- [23] O. Gruber, et al. *Physical review letters*, 74(21):4217, 1995.
- [24] J. Neuhauser, et al. *Plasma Phys. Control. Fusion*, 37(11A):A37, November 1995.
- [25] M. Wischmeier, et al. *Journal of Nuclear Materials*, 390–391:250–254, June 2009.
- [26] L. Aho-Mantila, et al. *Journal of Nuclear Materials*, 438, Supplement:S321–S325, July 2013.
- [27] S. Potzel, et al. *Journal of Nuclear Materials*,

- 438, Supplement:S285–S290, July 2013.
- [28] N. Asakura, et al. *Journal of Nuclear Materials*, 266–269:182–188, March 1999.
- [29] A. Hatayama, et al. *Journal of Nuclear Materials*, 290–293:407–412, March 2001.
- [30] B. Lipschultz. In *IAEA 1998*, Yokohama, Japan, 1998.
- [31] K. Borrass, et al. *Nucl. Fusion*, 44(7):752, July 2004.
- [32] W. Suttrop, et al. *Journal of Nuclear Materials*, 266–269:118–123, March 1999.
- [33] M. Bernert, et al. In *EPS 2013*, Helsinki, 2013.
- [34] F. Reimold, et al. *Journal of Nuclear Materials*, 2014. submitted.
- [35] B. Lipschultz, et al. *Journal of Nuclear Materials*, 266–269:370–375, March 1999.
- [36] T. W. Petrie, et al. *Journal of Nuclear Materials*, 241–243:639–644, February 1997.
- [37] A. Kallenbach, et al. *Journal of Nuclear Materials*, 290–293:639–643, March 2001.
- [38] A. Kallenbach, et al. *Plasma Phys. Control. Fusion*, 52(5):055002, May 2010.
- [39] T. W. Petrie, et al. *Nucl. Fusion*, 48(4):045010, April 2008.
- [40] A. Kallenbach. In *IAEA 2014*, pages EX/7–1, St. Petersburg, Russia, March 2014.
- [41] M. Weinlich. Technical Report IPP 5/64, Max-Planck Institut for Plasma Physics, Munich, 1995.
- [42] P. C. Stangeby. *J. Phys. D: Appl. Phys.*, 20(11):1472, November 1987.
- [43] H. P. Summers. <http://www.adas.ac.uk/manual.php>, 2004.
- [44] S. Potzel, et al. *Plasma Phys. Control. Fusion*, 56(2):025010, February 2014.
- [45] M. Weinlich and A. Carlson. *Contrib. Plasma Phys.*, 36(S1):53–59, 1996.
- [46] M. Weinlich and A. Carlson. *Physics of Plasmas (1994-present)*, 4(6):2151–2160, June 1997.
- [47] M. Bernert. *Analysis of the H-mode density limit in the ASDEX Upgrade tokamak using bolometry*. Thesis, Ludwig-Maximilian University Munich, 2013.
- [48] T. W. Petrie, et al. *Nucl. Fusion*, 37(3):321, March 1997.
- [49] M. E. Fenstermacher, et al. *Plasma Phys. Control. Fusion*, 41(3A):A345, March 1999.
- [50] T. Ishijima, et al. *Plasma Phys. Control. Fusion*, 41(9):1155, September 1999.
- [51] C. S. Pitcher, et al. *Journal of Nuclear Materials*, 220–222(0):213–217, April 1995.
- [52] M. Bernert, et al. *Review of Scientific Instruments*, 85(3):033503, March 2014.
- [53] A. Scarabosio, et al. *Nuclear Instruments and Methods in Physics Research Section A: Accelerators, Spectrometers, Detectors and Associated Equipment*, 623(2):667–671, November 2010.
- [54] R. L. Summers. *NASA TN D-5285*, volume 5285. National Aeronautics and Space Administration, 1969.
- [55] S. Potzel. In *PSI 2014*, Kanazawa, Japan, May 2014.
- [56] K. McCormick, et al. *Journal of Nuclear Materials*, 390–391:465–469, June 2009.
- [57] J. Wesson. *Wesson J. Tokamaks (3ed., Oxford, 2004)(K)(T)(755s).djvu*, volume 1. Clarendon Press, Oxford, 3 edition, 2004.
- [58] D. Carralero. In *APS Division of Plasma Physics Meeting Abstracts*, New Orleans, USA, November 2014.
- [59] D. D. Ryutov, et al. *Contributions to Plasma Physics*, 52(5-6):539–543, 2012.
- [60] N. Asakura, et al. *Journal of Nuclear Materials*, 415(1):S318–S321, August 2011.
- [61] H. D. Pacher, et al. *Journal of Nuclear Materials*, 390–391:259–262, June 2009.